Materialia 20 (2021) 101201

Contents lists available at ScienceDirect

Materialia

journal homepage: www.elsevier.com/locate/mtla

Full Length Article

Formation and 3D morphology of interconnected α microstructures in additively manufactured Ti-6Al-4V

Ryan DeMott[a,*], Nima Haghdadi[a], Ziba Gandomkar[b], Xiaozhou Liao[c,d], Simon Ringer[c,d], Sophie Primig[a,*]

[a] School of Materials Science & Engineering, UNSW Sydney, Sydney, NSW 2052, Australia
[b] Medical Imaging Science, Faculty of Medicine and Health, The University of Sydney, Lidcombe, NSW 2141, Australia
[c] Australian Centre for Microscopy & Microanalysis, The University of Sydney, Sydney, NSW 2006, Australia
[d] School of Aerospace, Mechanical and Mechatronic Engineering, The University of Sydney, Sydney, NSW 2006, Australia

ARTICLE INFO

Keywords:
3D EBSD
Titanium alloys
Phase morphology
Microstructure formation
Interconnectivity

ABSTRACT

Three-dimensional characterization methods, such as 3D electron backscatter diffraction (3D-EBSD), have been used to reveal phase transformation and microstructural evolution mechanisms in multi-phase materials such as steel or titanium alloys. While 3D techniques have enabled many findings in steels, fine dual phase microstructures in titanium alloys such as the basketweave structure have been challenging to resolve. Now, advances in 3D-EBSD methods using sectioning with a plasma focused ion beam have allowed in-depth analyses of fine α microstructures. We apply 3D-EBSD to investigate the microstructures formed in Ti-6Al-4V by electron powder bed fusion (E-PBF) using different scanning strategies. Basketweave, acicular, and colony microstructures are produced from linear, Dehoff, and random scanning strategies, respectively. Different types of 3D interconnectivity were revealed in each microstructure including within clusters of platelets in the basketweave microstructure, within a grain boundary allotriomorph in the acicular microstructure, and between platelets in colonies. These observations are discussed in terms of the formation mechanisms of interconnectivity, including sympathetic nucleation, impingement, and morphological instability. Morphological instability was found to potentially play a role in both the basketweave and colony structures while the interconnectivity in the acicular structure likely forms via sympathetic nucleation or impingement. This information allows for a more complete description of the phase evolution of Ti-6Al-4V during thermal cycling in E-PBF than previously available and represents new insights into the complex branching reported in different titanium microstructures.

1. Introduction

Three-dimensional microscopy techniques, while far from new, have lately gained increased interest due to improvements in resolution and computational reconstruction and visualization techniques [1]. 3D imaging and analysis have enormous potential to provide crucial insights into the true morphology and evolution of complex microstructures. These techniques can now be applied to reveal the microstructural evolution of titanium alloys, which can form a variety of phases in highly complex 3D morphologies under certain processing conditions. This potential has been demonstrated previously in answering several open questions within the field of steels, which undergo a similar array of phase transformations and form similar complex structures, though generally on a coarser scale.

In case of steels, these include the morphology and origin of proeutectoid Widmanstätten ferrite and cementite, the origins of bainite/acicular ferrite, and the formation mechanism of pearlite. Deep etching [2] and serial sectioning [3] revealed how proeutectoid cementite plates in fact originated at an austenite grain boundary (GB) even when they appeared to be intragranular, as well as dendrite-like 3D morphologies within cementite films on austenite GBs. A major controversy in this area was whether Widmanstätten side plates formed on GB allotriomorphs via sympathetic nucleation [4] or branching due to morphological instability [5]. Sympathetic nucleation is the nucleation of a precipitate at the interface of another precipitate of the same phase in order to continue a phase transformation after the phase interface can no longer move, or to replace the high energy phase interface with a lower energy GB [4,6–8]. Morphological instability can occur when perturbations in a migrating phase boundary cause the interface to become unstable and form branches [9–11].

Though in situ experiments and many observations of low angle grain boundaries (LAGBs) between side plates have contributed to the conclusion that sympathetic nucleation generally dominates in this case

* Corresponding authors.
E-mail addresses: r.demott@unsw.edu.au (R. DeMott), s.primig@unsw.edu.au (S. Primig).

https://doi.org/10.1016/j.mtla.2021.101201
Received 9 August 2021; Accepted 20 August 2021
Available online 24 August 2021

[12–16], several studies utilizing 3D characterization provided important information about the true 3D morphology of Widmanstätten ferrite [17–21]. Mangan et al. [17] showed how plates can intersect each other in 3D, either blocking or growing past each other, and also that when plates grow near each other, interactions between the diffusion fields of the growing plates (or soft impingement) caused the plates to bend away from their ideal habit plane. Kral et al. [18] provided an updated version of a classic scheme for classifying precipitate morphologies [22] to take the full 3D morphology into account. Another example is the serial sectioning of Widmanstätten in a meteorite (the original source of the term Widmanstätten) to observe cases of plates intersecting [23].

In the case of bainite/acicular ferrite, there is ongoing debate over whether the phase transformation is diffusive, displacive, or a combination of the two [24] (often called a diffusive-displacive transformation [25]). 3D characterization has provided key insights in this area, including the morphologies of nanobainite [26], coalesced bainite [27], and interwoven acicular bainite [28]. Kang et al. used 3D-EBSD to show how different bainite morphologies can result from diffusive vs displacive processes [28] and Motomura et al. paired elemental mapping with serial sectioning to show the role of diffusion in forming acicular bainite [29]. Acicular plates have often been observed in complex, interwoven patterns in 3D [28–32] with sympathetic nucleation often cited as mechanism for forming interwoven structures [30–34].

A pioneering serial sectioning experiment by Hillert [35] proved that pearlite colonies actually only consist of a single crystal each of ferrite and cementite, branched and woven together. This enabled understanding how pearlite forms by branching via morphological instability and ledge-wise growth [36–40] and the original micrographs from [35] have even been digitized to produce a 3D reconstruction of the original colony [41].

These results set the scene for 3D characterization to provide similar insights into the microstructural evolution of titanium alloys, due to the wide array of microstructures and phase transformations that occur. Pure titanium has a body-centered cubic crystal structure (β phase) at high temperature and hexagonal close-packed crystal structure (α phase) at room temperature. Titanium alloys generally consist of a mix of the two phases at room temperature with the fractions determined largely by the amount of β stabilizing elements such as vanadium or molybdenum. Phase transformations can be martensitic, diffusional, diffusive-displacive, massive, or pseudo-spinodal depending on the alloy and processing conditions [42–47]. Microstructures commonly seen in α+β alloys such as Ti-6Al-4V include colony α, where parallel α lamellae of the same crystal orientation are arranged in sheaves or colonies; basketweave (Widmanstätten α), where α platelets of multiple orientations are woven together in a complex 3-dimensional fashion; and α' martensite, consisting of fine acicular laths arranged similarly to the basketweave microstructure. Equiaxed and bimodal microstructures are also common [42]. This considerable complexity is exacerbated by additive manufacturing (AM) methods such as electron beam powder bed fusion (E-PBF) which result in significant anisotropy and complicate the phase evolution with repeated thermal cycling. AM microstructures in Ti-6Al-4V generally consist of fine α microstructures with different morphologies within large, columnar β grains.

One particular open question is whether branching via morphological instability plays any role in the evolution of titanium microstructures, especially in the case of the formation of Widmanstätten side plates forming on GB allotriomorphs [48–51]. While these side plates have often been attributed to sympathetic nucleation [7,52,53], there is evidence for morphological instability as well [49,51] and one study suggests that both may occur [48]. Morphological instability has been observed or modelled in titanium in several other contexts, including branching growth of a GB-α precipitate [54], formation of sheafs of parallel platelets [55], and secondary branches off of Widmanstätten side plates [50]. Additionally, it has recently been reported that α grains within the basketweave microstructure in additively manufactured (AM) Ti-6Al-4V exhibit extensive interconnectivity in 3D which may be indicative of branching behavior [56].

Though some 3D characterization has been employed on titanium alloys already [54,57,66–69,58–65], it has often been limited to relatively low-resolution techniques, such as serial sectioning via mechanical polishing [69], high-energy x-ray diffraction [67,68], and reconstructions of coarse features such as equiaxed microstructures [61], prior β grains [67], or low-density α laths in near β alloys [62]. The recent development of the plasma based focused ion beam (P-FIB) now allows for the collection of large volumes at high resolutions [70]. When paired with a high-speed electron backscattering diffraction (EBSD) detector, this allows for the collection of large, high-resolution 3D datasets with crystallographic information. This can provide details on the 3D morphology of the fine acicular and basketweave microstructures in α+β alloys which are otherwise very challenging to resolve with other 3D characterization methods [56].

The microstructural evolution of Ti-6Al-4V during E-PBF has been investigated previously [71–73] but the general phase transformation route proposed ($\ell \rightarrow \beta \rightarrow \alpha' \rightarrow \alpha+\beta$) is insufficient to account for the arrays of microstructures produced by different scanning strategies [74–76] or the 3D interconnectivity [56]. Following our extensive 2D EBSD characterization of the effects of E-PBF scanning strategy on microstructural evolution in Ti-6Al-4V [74,77], and a feasibility study employing 3D-EBSD on basketweave Ti-6Al-4V [56], two main areas were identified that would benefit from an in-depth 3D analysis. The first was the effect of scanning strategy on variant selection behavior and grain boundary network in 3D which was the subject of our previous publication [78]. This study revealed that the variant selection behavior is strongly dependent on the scan strategy due to differences in the thermal profile. The variant selection behavior was dominated by two different types of self-accommodation in the linear and Dehoff samples and dominated by prior β grain boundaries in the random sample. The second, which is presented here, is the 3D morphology and interconnectivity of fine α microstructures and its role in microstructural evolution during E-PBF. We present analyses of the grain morphologies and interconnectivity observed in Ti-6Al-4V processed by E-PBF using three different scan strategies to produce three different characteristic microstructures. This provides critical insights into two important gaps in the state of the art: first, a better understanding of the origins of interconnectivity in titanium microstructures in general and what role branching plays in microstructural evolution, and second a more comprehensive model of the microstructural evolution during E-PBF using different scanning strategies. The raw data used here is the same as that presented in [78], with new and distinct analysis presented here.

2. Methods

As previously described [56,74,77,78], blocks were built using an ARCAM EBM system using three different scan strategies: a linear raster, a periodic spot melt (Dehoff) and a random spot melt. A 3D-EBSD data set was collected from each sample from a location chosen based on extensive 2D observations [74,77] to represent three distinct microstructures. The center of the linear build is composed of a basketweave structure; the bottom of the Dehoff build is composed of an acicular, martensite-like microstructure; and the center of the random build is composed of a colony microstructure. A representative 2D EBSD map of each of the microstructures is shown in Fig. 1. The maps shown are inverse pole figure (IPF) maps which represent the crystal direction aligned with the build direction overlaid with image quality to show the internal structure of the colonies in the random sample (Fig. 1(c)). The inset IPF color triangle in Fig. 1(a) applies to all IPF maps throughout the remainder of the manuscript.

The 3D-EBSD datasets were collected using block-face serial sectioning in a Xe+ plasma FIB, controlled using the Auto Slice and View software and Aztec 4.0 EBSD collection software. The slice thickness was 50 nm using rocking milling to reduce curtaining effects, and EBSD was

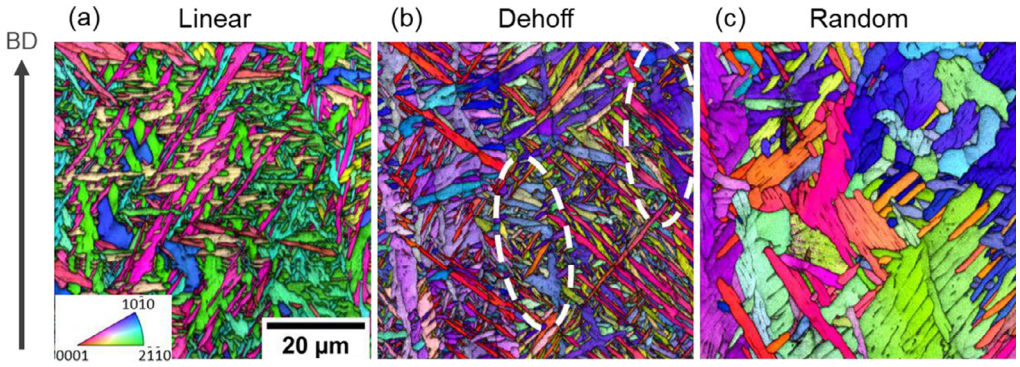

Fig. 1. Inverse pole figure (IPF) maps with image quality overlaid for (a) the basketweave microstructure in the center of the linear build, (b) the acicular microstructure in the center of the Dehoff build with large grain boundary α indicated by dashed white circles, and (c) the colony structure in the center of the random build.

collected every two slices with a step size of 100 nm for a final voxel size of $(100\ \text{nm})^3$. The volumes collected for the linear, Dehoff, and random samples were $13.6 \times 29.4 \times 31.3\ \mu\text{m}^3$, $22.1 \times 24.1 \times 36.3\ \mu\text{m}^3$, and $23.5 \times 31.6 \times 37.0\ \mu\text{m}^3$, respectively. Reconstruction and analysis were performed with the DREAM.3D software package [79] and further analysis was carried out with the MTEX toolbox for Matlab [80]. Briefly, the reconstruction consisted of alignment, clean-up, and segmentation with a grain tolerance angle of 2° The raw indexing rate for the linear, Dehoff, and random samples, respectively were 74, 66, and 90%. An in-depth description of the reconstruction and analysis methods will follow in a separate publication. The linear dataset by random chance happened to contain a prior β grain boundary though the center of the volume and the other two datasets were placed to contain prior β grain boundaries using BSE imaging prior to milling out the pillar for sectioning.

Many grains included multiple platelets spread over different planes. In order to calculate how many platelets each grain had, we used M-estimator Sample Consensus (MSAC) algorithm [81], a variant of the Random Sample Consensus (RANSAC) [82], provided in MATLAB's Computer Vision Toolbox. The RANSAC algorithm considers the desired fitting model with an unknown set of parameters and estimates them while maximizing the number of inliers within a pre-specified distance (7 voxels in this case). The RANSAC treats all inliers uniformly without any penalty while the MSAC utilizes a cost function where a penalty is assigned to an inlier based on the extent it satisfies the required functional relation [81,82]. Here we assumed our fitting models are planes. We iteratively fitted a series of planes to each grain in the linear and Dehoff data sets using the MSAC algorithm. In the first iteration, the first plane, with the highest number of points, was detected and all points belonging to the fitted plane were excluded from the data. In the next iteration, the second plane was fitted to the remaining points. The iterative process terminated when less than 5% of the data was remained. For monolithic platelets, or grains containing only a single platelet, only one plane should be required to fit more than 95% of the voxels, while grains with multiple platelets should require several iterations to fit a plane to each platelet. This provides a metric for how interconnected each grain is based on how many planes need to be fitted to include most of the data.

3. Results

3.1. Linear (basketweave)

An overview of the full volume of the linear dataset is shown in Fig. 2(a). The structure is composed generally of platelets in a basketweave configuration, and the prior β GB can be seen running though the center of the sample. The 3D perspective of the basketweave microstructure reveals that the structure is more complex and interconnected than is apparent from a single 2D section.

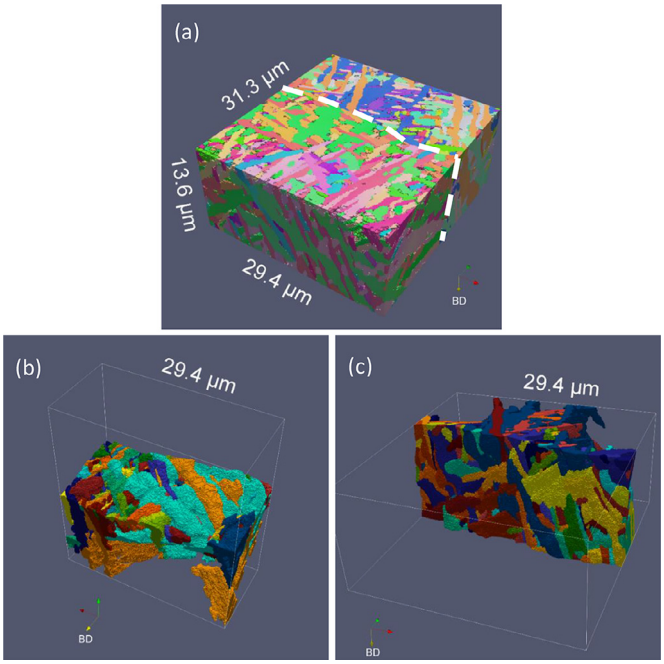

Fig. 2. (a) The full volume of the linear 3D EBSD dataset in IPF color showing the basketweave microstructure in both prior β grains and no apparent grain boundary α. The prior β grain boundary is indicated by the dashed line. (b, c) All of the grains intersecting on each side of the prior β grain boundary surface in the linear dataset shown in unique grain color.

As the presence or absence of grain boundary α is important for the microstructural evolution, it is useful to examine the surfaces of the prior β grain boundaries to see what role GBα may have played. Fig. 2 (b,c) and supplemental video 1 show all the α grains which intersect the prior β grain boundary on either side of the boundary. The platelets all intersect the boundary along their growth directions without seeming to grow along the boundary surface or cover a large area. The apparent relatively large boundary area occupied by the light blue grain is a result of that variant having a habit plane near to the boundary plane. Thus, in this sample, there does not appear to be any so called allotriomorphic α. Though this is only a small section of one prior β grain boundary, this observation is consistent with the 2D EBSD scans of this microstructure in previous work [74,77] which found very little GBα in the basketweave structure.

The complexity of the grain structure can be seen more readily in Fig. 3 and supplementary video 2, where (a-d) show examples of very large, interconnected grains consisting of multiple platelets of the

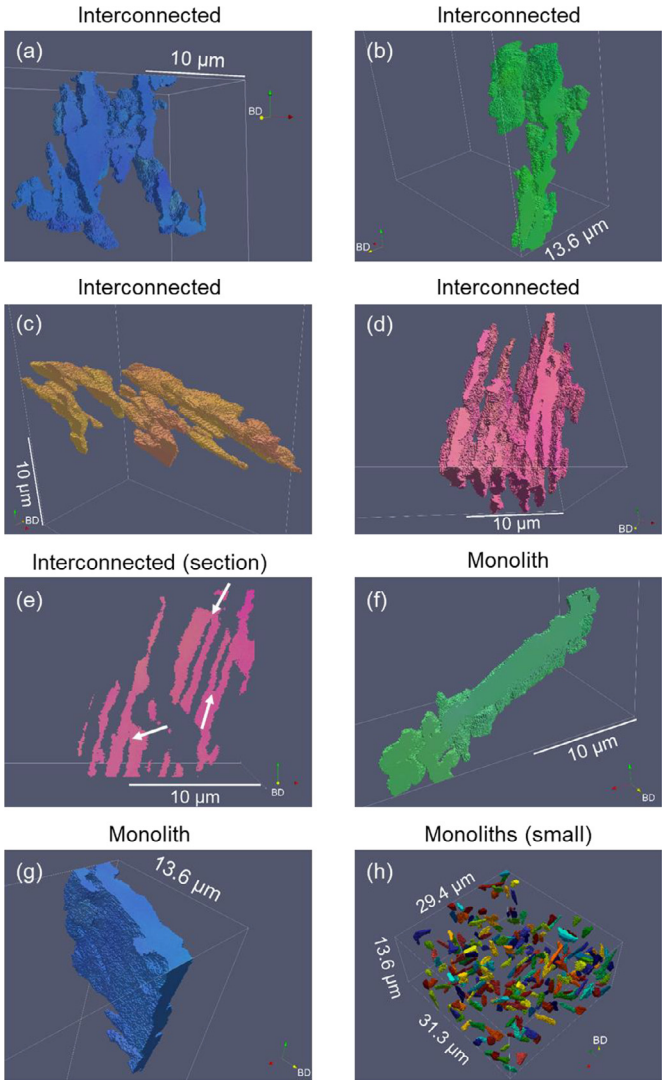

Fig. 3. A collection of representative grains from the linear dataset including (a-d) highly branched/interconnected grains, (e) a cross section of the grain in (d) with arrows indicating branching points, (f-g) large, monolithic grains, and (h) a selection of small monolithic grains. (a-g) are shown in IPF color and (h) is shown in unique grain color.

same orientation that are connected via bridges and branching points throughout the volume. Fig. 3(e) is a cross section through the grain in (d) where several of the bridges and branching points between adjacent platelets can be seen and are marked with arrows. Although these highly branched grains make up the majority of the volume, there are some monolithic grains as well (Fig. 3(f) and (g)). Additionally, there are many small grains with a range of shapes including equiaxed, rods, and platelets. They are generally elongated along the growth direction of their particular variant. A subset of these small grains with volumes between 1 and 2 μm^3 are rendered in Fig. 3(h) in unique grain color to provide a sense of their shape and distribution.

3.2. Dehoff (acicular)

The full volume of the Dehoff sample is shown in Fig. 4(a). The volume is mostly from one prior β grain with a small amount from a second prior β grain in one corner. The microstructure can be seen to contain many fine α plates and one large, interconnected cluster along the prior β grain boundary.

The α grains along the prior β grain boundary are shown in unique grain color in Fig. 4 (b,c) and supplementary video 3. A number of small

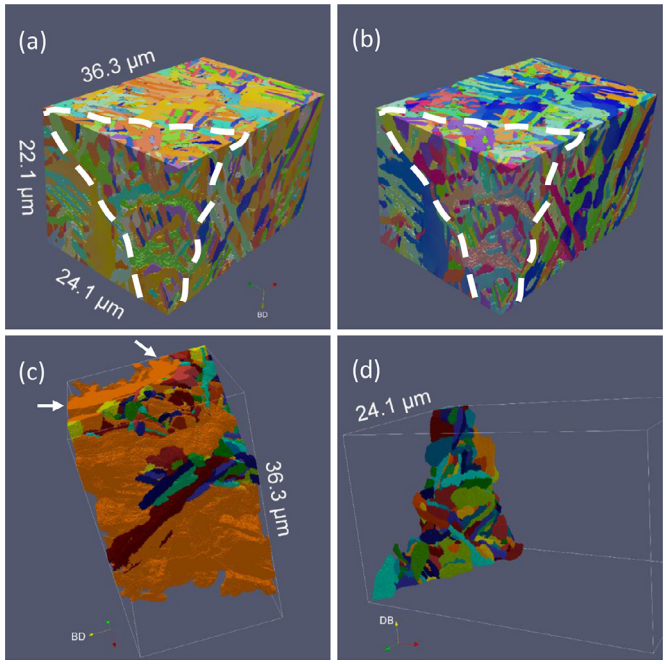

Fig. 4. (a-b) The full volume of the Dehoff 3D EBSD dataset in IPF color (a) with respect to the build direction and (b) with respect to the Y direction (green axis). The prior β grain boundary is indicated by the dashed line. (c-d) All grains intersecting each side of the prior β grain boundary surface in the Dehoff dataset are shown in unique grain color. Arrows show where the very large cluster curves, likely following the prior β GB outside of the collected volume.

platelets intersect the boundary, but a large portion of the boundary surface on the side of the larger prior β grain is taken up by one very large grain. Additionally, the large grain can be seen to curve where it intersects the edge of the volume, suggesting that it continues to follow the boundary surface outside of the collected volume as shown by the arrows in Fig. 4(c). This suggests that the large, interconnected grain may have grown from the prior β grain boundary from a GBα precipitate. While it is difficult to generalize the behavior along prior β GBs based on this small area of GB surface, this structure is similar to some observed in 2D EBSD scans of the acicular microstructure at the bottom of the Dehoff sample indicated by the dashed circles in Fig. 1(b).

This microstructure contains many more monolithic, flat, martensite-like plates, some examples of which are shown in Fig. 5(b-d) and supplementary video 4. As in the linear sample, there is also an array of small grains of assorted shapes, generally elongated along the growth direction of their variant. The Dehoff sample also contains some interconnected structures. This is primarily one very large grain consisting of many platelets which are all interconnected. This grain spans nearly the entire volume of the larger prior β grain and contains platelets which have grown in two different directions and is shown in Fig. 5(a). These different growth directions may represent impingement of distinct variants.

In contrast to the linear sample, the Dehoff sample contains relatively large intragranular misorientations which can be seen in the changes in IPF color both within the large, interconnected cluster as well as the monolithic platelets.

3.3. Random (colony)

The full volume of the random sample is shown in Fig. 6(a). The grains are noticeably larger than the other samples and are generally colonies of parallel platelets. The thin β ribs which delineate the individual lamellae of the colonies can be seen as areas of low band slope

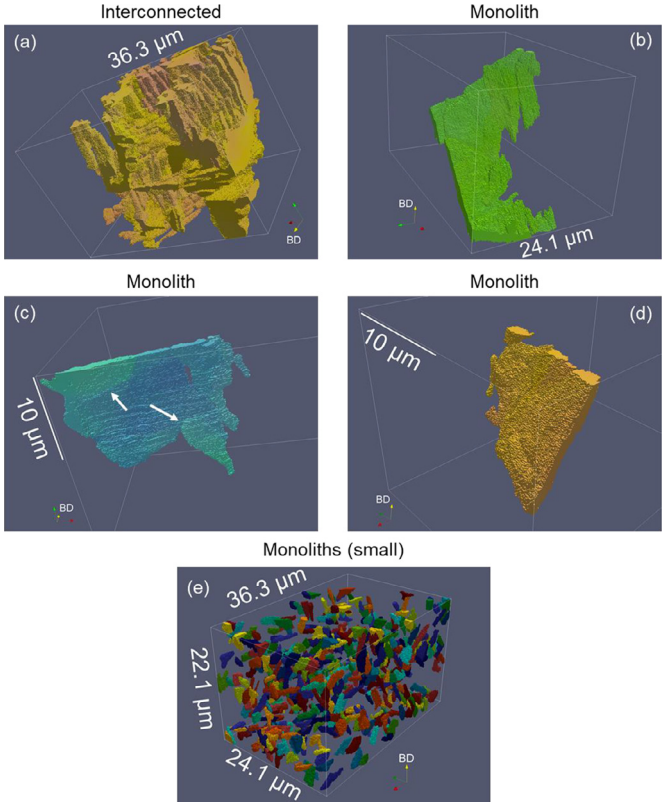

Fig. 5. A collection of representative grains from the Dehoff dataset including (a) a very large and complex grain, (b-d) large, monolithic grains, and (e) a selection of small monolithic grains. (a-d) are shown in IPF color and (e) is shown in unique grain color. Arrows in (c) show LAGBs in one of the monolithic platelets.

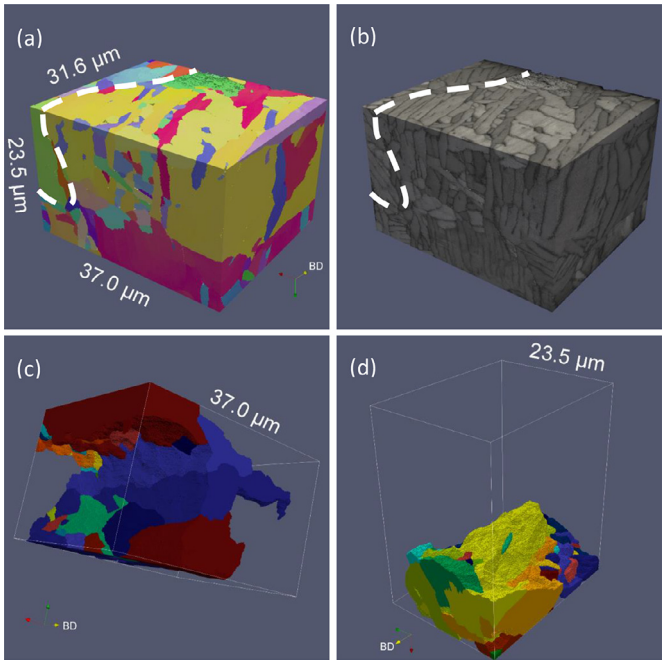

Fig. 6. (a-b) The full volume of the random 3D EBSD dataset (a) in IPF color to show the orientation of the colonies and (b) in band slope to show the internal structure of the colonies. The prior β grain boundary is indicated by the dashed line. (c-d) All of the grains intersecting each side of the prior β grain boundary surface shown in unique grain color.

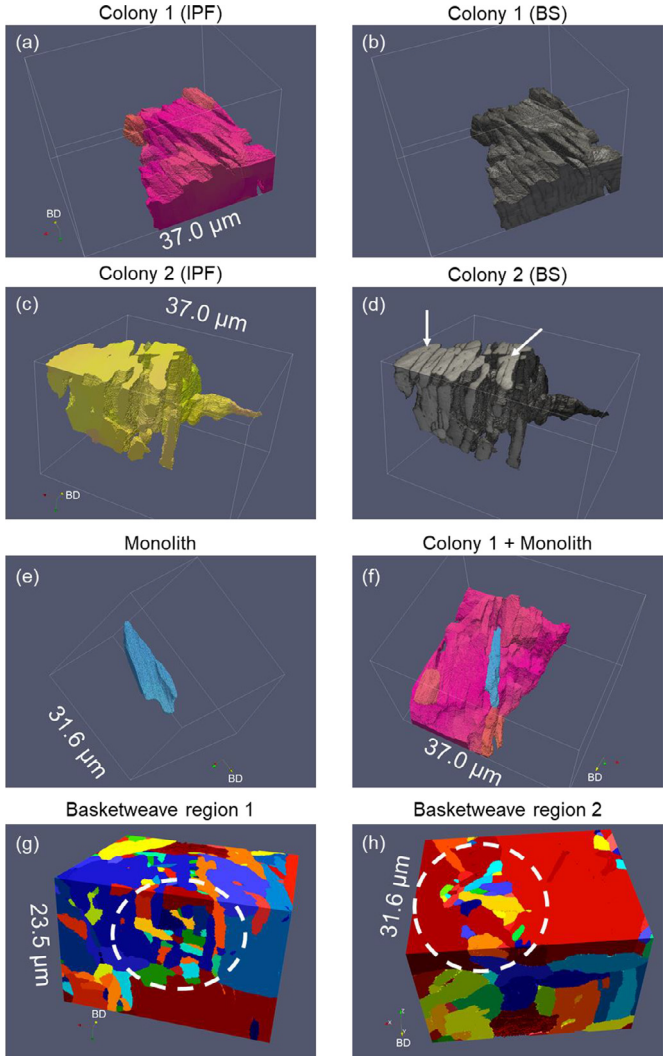

Fig. 7. (a-d) 2 examples of α colonies from the random dataset in (a,c) IPF color and (b,d) BS. (e) a single α platelet. (f) the same α platelet embedded in the colony shown in (a). (g,h) two basketweave-like regions (dashed circles) in the random sample shown in unique grain color.

(BS) in Fig. 6(b). The prior β GB surfaces are shown in Fig. 6 (b,c) and supplementary video 5.

The colonies which intersect the boundary can be seen to cover large areas of the GB surface and follow the curve of the surface, suggesting that the colonies may have nucleated as GB α and subsequently grown into the prior β grains. As mentioned before, though this is a very limited dataset with respect to the prior β GB behavior, the result is consistent with extensive observations in 2D of colonies growing from GB α films [74].

Two representative examples of colonies are shown in Fig. 7 (a-d) and supplementary video 6. The colonies can be seen to have a significant amount of branching between the lamellae within each colony as indicated by the arrows in Fig. 7(d). There are also a few smaller, monolithic grains in a few areas which appear more basketweave-like. Fig. 7(e) and (f) show an example of one such platelet which is embedded almost entirely within one colony. Two examples of areas which appear more basketweave-like are shown in Fig. 7(g) and (h).

3.4. Interconnectivity

To examine whether the interconnectivity in the basketweave microstructure of the linear sample and the acicular microstructure in the

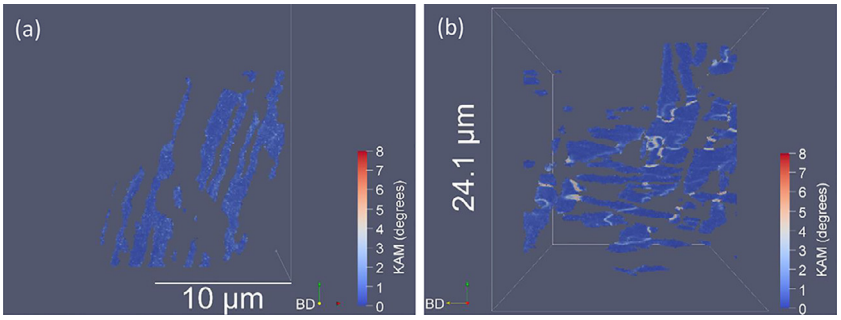

Fig. 8. Kernel average misorientation (KAM) maps of cross sections from branched grains in (a) the linear dataset and (b) the Dehoff dataset.

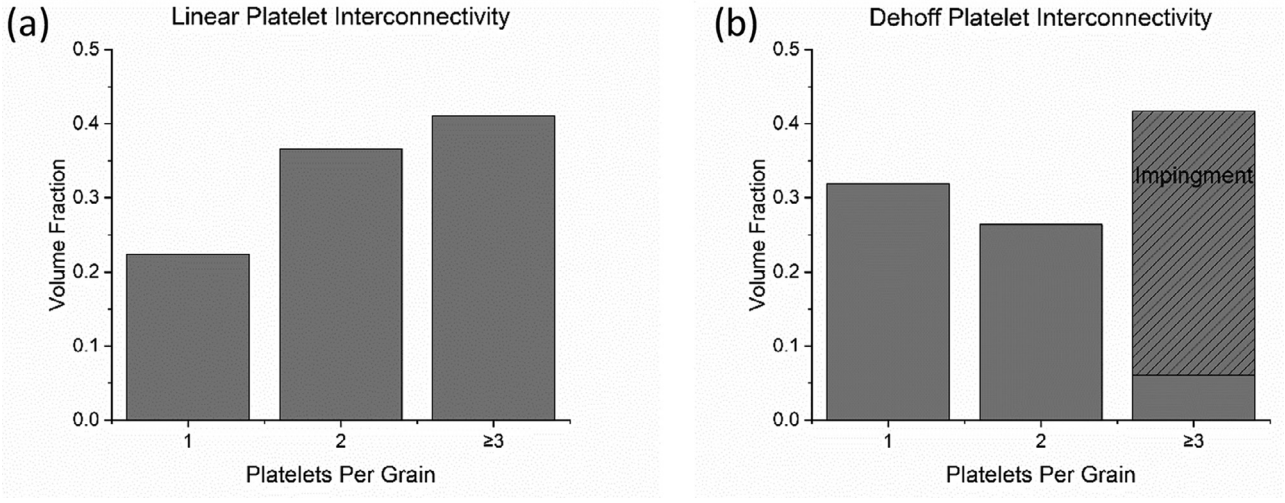

Fig. 9. Interconnectivity of linear (a) and Dehoff (b) samples as indicated by the volume fraction of grains consisting of 1,2, or 3 or more platelets as calculated by the MSAC algorithm which fits the points in each grain to a series of planes until 95% of the points are assigned to a plane. A large portion of the grains containing 3 or more platelets in the Dehoff sample is labeled as impingement as it is from the single large cluster in Fig. 5(a) which contains many LAGBs.

Dehoff sample results from the same phenomenon, the kernel average misorientation (KAM) with a 3 × 3 × 3 voxel kernel size was calculated for both samples. Fig. 8(a) shows the KAM within a slice through one of the interconnected grains in the linear sample (Fig. 3(d)) while Fig. 8(b) shows the KAM within a slice through the highly interconnected grain from the Dehoff sample (Fig. 5(a)) (supplemenary video 7). The grain from the Dehoff sample contains many LAGBs between different platelets, suggesting that this may have formed as a result of hard impingement or sympathetic nucleation, while the grain from the linear sample does not appear to have any LAGBs, indicating that this may be a true branching behavior.

The interconnectivity of the linear and Dehoff samples is summarized quantitatively in Fig. 9. This is accomplished by classifying grains identified in the orientation-based segmentation by the number of individual platelets they contain. About 41% of the volume of the linear sample is composed of grains or clusters consisting of 3 or more platelets and 37% of the volume is composed of grains consisting of two platelets while only 22% of the volume consists of monolithic platelets. In the Dehoff sample, 32% of the volume is composed of monoliths and 26% is composed of duplets. The algorithm identified a large volume composed of three or more platelets; however, this is almost all from the cluster shown in Fig. 5(a) and Fig. 8(b), where the apparent branching may be a result of impingement as discussed above. There are three smaller clusters of the same variants which are likely connected to it outside the volume and one grain which is composed of two monolithic platelets of different variants which were segmented as a single grain due to intragranular misorientations blurring the boundary between them (supplementary figure 1). If these grains are ignored, the volume fraction of the Dehoff sample composed of highly branched grains is only 6%.

4. Discussion

The three samples studied in this work represent distinct microstructures as a result of the different thermal histories of the three different scan strategies. All microstructures exhibit some degree of interconnectivity when examined in 3D. However, differences in the nature of the interconnectivity suggest that different phenomena may be at play. Understanding the nature of each phenomenon can shed light on how each microstructure may have formed during its respective thermal history. Thus, in the following discussion, we will first examine possible origins of the interconnectivity and analyze which may be operating in each sample, and then discuss the likely sequence of microstructural evolution that led to the formation of each final microstructure. These findings will then be compared to the similar phenomena and 3D characterization studies in steels.

4.1. Origins of interconnectivity

Three possibilities exist for the interconnectivity between α laths observed in this study. The first is coalescence or impingement of initially separate platelets as they coarsen. This would most likely be marked by a LAGB where the two platelets meet in the case of coalescence/hard impingement or a thin layer of β in the case of soft impingement. Another possibility is sympathetic or autocatalytic nucleation, where one α platelet nucleates at the interface of another in order to minimize boundary energy [7] or local strain energy [8], respectively. Since sympathetic nucleation is driven by replacing the α-β interface with a lower energy α-α GB, it will most likely favor nucleation of a platelet of the same variant as the substrate platelet, and in turn form a LAGB [7]. Autocatalysis on the other hand will often result in the formation of clusters

of three variants sharing <11$\bar{2}$0> directions [83]. The third possibility is through branching via interfacial instabilities. This is often observed in the case of side plates forming off of GBα films [49]. The formation of branches off of growing side plates has recently been modelled by Sun et al. [50] using phase field. Their results suggest that the branches occur when a side plate is not growing along its ideal growth direction, to correct for the deviation. Additionally, experimental evidence of branching in the formation of colony like sheafs of platelets has been reported by Choudhuri et al. [55] along with phase field modeling which shows that growth ledges provide sufficient perturbations in the inter-phase boundary to allow branches to grow.

While the formation of the colonies in the random sample is relatively straightforward, it is worth examining as it has not been discussed in previous literature on the microstructural evolution of Ti-6Al-4V during E-PBF, and branches within colonies have rarely been reported [55].

The linear and Dehoff samples are more difficult to interpret, due to the high degree of complexity within the basketweave and acicular structures. While both microstructures look similar and contain a certain degree of interconnectivity, a 3D perspective confirms that these are in fact distinct microstructures, as previously indicated by their differing variant selection behavior [74,77]. More detailed quantitative information about the branching behavior than that presented in Fig. 9 could provide more insight, but is currently impractical due to the difficulty in isolating individual platelets in the clusters of multiple platelets which are segmented as single grains. If the large, branched grains could be sub-segmented to identify individual platelets, their spatial orientation and number of branching points could be calculated.

4.1.1. Linear (basketweave) interconnectivity

The basketweave microstructure in the linear sample is largely composed of clusters of interconnected platelets of each variant woven together in 3D. The morphology of the interconnected platelets suggests that the branches have most likely formed via interfacial instability. This type of branching has never before been observed in the formation of a basketweave microstructure, but the lack of any LAGB at branching points (Fig. 8(a)) is evidence against impingement or sympathetic/autocatalytic nucleation. During the formation of a basketweave microstructure, the presence of multiple platelets of different variants could often result in interactions between diffusion fields (soft impingement [84]), forcing a growing platelet away from its ideal habit plane [17]. This could create a sufficient perturbation to allow a branch to form in order to correct the growth direction and allow for the grain to continue growing past the obstacle [5,50].

Interactions between growing platelets have been studied little, however, Rajab and Doherty [85,86] studied the growth and intersection of plate-like precipitates in Al-Ag alloys and found that impingement between plates spurred the formation of growth ledges to facilitate growth out of the habit plane. In titanium alloys, impingement between α platelets is most likely soft impingement, where the precipitates will stop growing toward each other once their diffusion fields overlap [87–91]. Soft impingement was suggested by Townsend and Kirkaldy [5] as the mechanism behind a platelet curving away from its crystallographic habit plane in steel. Thus, branching may occur in the formation of basketweave to accommodate soft impingement when platelets of different variants meet. When a growing platelet encounters an obstacle, it may start growing out of its habit plane, and then form a new branch to correct for the deviation in habit plane. However, the lack of LAGBs or low band may not be sufficient by itself to definitively rule out hard impingement/coalescence.

4.1.2. Dehoff (acicular) interconnectivity

The interconnectivity within the acicular microstructure in the Dehoff sample, however, is almost wholly accounted for by a single very large cluster of platelets from two variants which may be associated with a GBα. There are many LAGBs within this cluster. Based on this evidence, it seems that the Dehoff sample could most accurately be described as consisting of large flat platelets embedded within a large cluster of platelets which are interconnected via sympathetic nucleation or possibly hard impingement. This large cluster/grain is apparently associated with GB α and is analogous to the region in 2D along the prior β GB circled in Fig. 1(b).

4.1.3. Random (colony) interconnectivity

The simplest case is the colony microstructure in the random sample, where branches within individual colonies are clearly visible without the additional complication of other variants in the vicinity. These branches appear quite similar to those observed in other lamellar structures such as pearlite [41], and there is no evidence of any sort of boundary at the branching points. This indicates that branching via instability is likely operative, similar to the accepted method for pearlite growth except that in this case it is simply α colonies growing in a β matrix rather than a eutectoid transformation. Impingement may be dismissed as the so many platelets of the same variant nucleating independently would be highly unlikely. Sympathetic nucleation is also unlikely due to the lack of any visible boundaries at the branching points [4,7]. With the right growth conditions, growth ledges could be sufficient perturbations to lead to branching [55]. Additionally, if a colony is growing around a pre-existing platelet, such as the one in Fig. 7(e), the interactions between the diffusion fields or strain fields of the pre-existing platelet and the growing colony could lead to interfacial instability.

4.2. Microstructural evolution during E-PBF

Now that the 3D morphology and interconnectivity have been discussed, it is of interest to link this to the phase transformations that each sample underwent. It is largely accepted that during E-PBF, Ti-6Al-4V first forms β upon solidification and then transforms to α' as it rapidly cools. The α' then transforms to α+β during subsequent thermal cycles [71,73]. But, what exactly happens during the thermal cycling is complex, and the microstructural evolution in these samples is more complex than α' formed on the initial cooling decomposing to α+β in place as in [73]. It is evident from the three unique final microstructures that the three scanning strategies studied here can produce different routes of microstructural evolution [74,77,78]. All three microstructures observed here exhibit distinct 3D morphologies and interconnectivity/branching behaviors that can only arise from the thermal cycling experienced by each point in the build after its initial melting. The 3D morphology, when considered along with observation from previous 2D and 3D analyses of the final microstructures, can allow a general outline of the microstructural evolution in each case. The relevant observations are summarized in table 1. Based on these points, schematics of potential transformation routes for the formation of each microstructure resulting from its respective scan strategy are presented in Fig. 10 and discussed in detail below. The final microstructural schematics can be compared to Fig. 1 to see how the proposed mechanisms lead to structures similar to the observed final microstructures.

4.2.1. Linear (basketweave) evolution

The significant degree of interconnectivity in the basketweave microstructure in the linear sample indicates that it has transformed considerably from the acicular structure which would have formed during the martensitic transformation on the first cooling cycle. There are two possibilities for how this might have occurred: One is that the α' transformed back to β on a subsequent reheating cycle and then transformed into the α+β basketweave by nucleating new variants intragranularly via autocatalysis (Fig. 10(a)). In this case, branching could occur either by impingement or as a result of surface instability when interactions with neighboring platelets force a growing platelet out of its ideal growing condition. The lack of LAGBs and change in VS behavior observed in the linear sample support this route [7,83,92]. However, the lack of GB allotriomorphs is evidence against the transformation back to β.

Table 1
Relevant observations of the three microstructures formed from the three scanning strategies which provide insight into the microstructural evolution.

Microstructure	Linear Basketweave	Dehoff Acicular	Random Colony
GB allotriomorphs	No	Yes	Yes
3D morphology	Interconnected platelets	Isolated laths in interconnected allotriomorph side plates	Colonies with internal branching
Intragranular misorientation	Moderate	High	Low
Variant selection behavior [74,77,78]	Self-accommodation (dominance of type 2 (60° <11$\bar{2}$0>) clusters)	Self-accommodation (dominance of type 4 (63.26° <$\bar{1}$0 5 5 3>) clusters)	Dominance of prior β grain boundary
Transformation back to β interconnectivity mechanism	Possible Impingement if not from β Maybe instability if from β	Possible partial Sympathetic nucleation/impingement	Mostly Instability

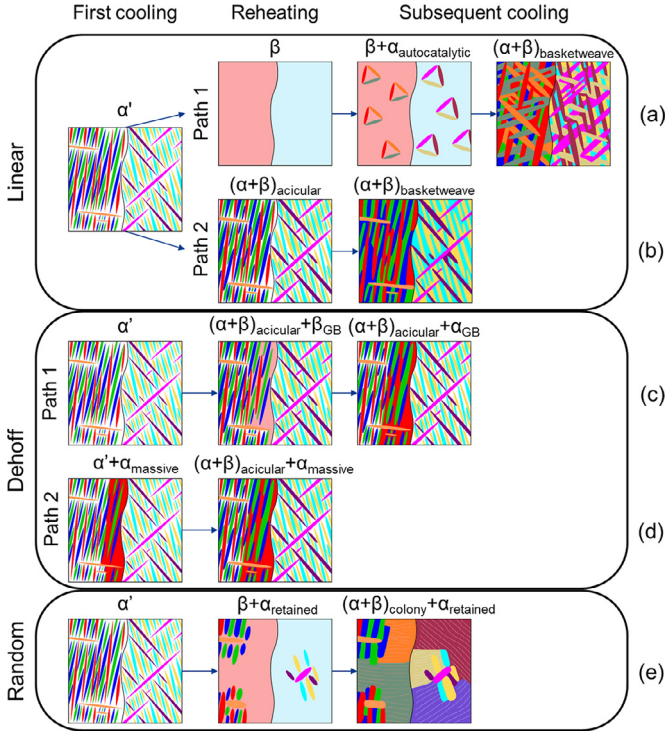

Fig. 10. Schematics of phase transformation routes which likely produced the microstructures observed in the linear, Dehoff, and random samples. Two possible paths for the linear sample include path 1: acicular α' transforms fully back to β before nucleating new α variants which form a basketweave structure via branching growth (a), or path 2: acicular α' coarsens as it decomposes to the equilibrium α+β structure and eventually forms an interconnected basketweave via impingement (b). Two possible paths for the Dehoff sample include path 1: a region of α' near a prior β GB transforms back to β and then transforms into α_{GB} which fills around the remaining acicular laths (c), or path 2: acicular α' and massive α form at the same time and the α' decomposes to acicular α+β (d). In the random sample, acicular α' transforms most of the way back to β which transforms into α+β colonies surrounding the retained α platelets (e). The colors used here represent different α variants, but not specific orientations.

The $\beta \rightarrow \alpha$ diffusional transformation often involves nucleation at grain boundaries, though this is not always the case [93–95] and the unique thermal environment of E-PBF may allow for nucleation to occur intragranularly. It is also possible that nucleation still occurred at the grain boundary, with growth occurring into the grain rather than along the boundary to form an allotriomorph [96].

The other possibility is that the acicular α' transformed directly into the α+β basketweave via decomposition in place and coarsening (Fig. 10(b)). This is the same transformation route proposed in [73]. In this case, interconnectivity could only form from impingement of the original laths as they coarsen. The lack of LAGBs in the interconnected grains, and the previously observed change in variant selection behavior are both evidence against the case of the α' decomposing in place and coalescing. However, the lack of GB allotriomorphs suggests that a transformation back to β may not have occurred and the change in variant selection behavior might be explained by a preferential growth of certain variants rather than nucleation of new ones.

Measurement or modeling of the thermal cycling during E-PBF of the different scanning strategies, as has been done for other AM methods previously, would allow for a definitive answer as to which transformation pathway occurs [97–99]. While this is outside the scope of the current study, it will be pursued in the future.

4.2.2. Dehoff (acicular) evolution

The acicular microstructure in the Dehoff sample consists of large monolithic platelets surrounded by a very large, interconnected grain. The monolithic platelets were likely formed during the initial martensitic transformation. During a later thermal cycle, a large portion of the volume near the prior β GB may have transformed back to β, while some of the martensitic laths were retained (though they likely relaxed to equilibrium α as V diffused out into the growing β). Then the secondary β transformed back to α diffusionally, starting as a GB allotriomorph and filling in around the retained laths via sympathetic nucleation of new side plates (Fig. 10(c)).

Another possibility is that the interconnected grain formed via a massive transformation starting at the prior β GB either in the same cycle as the martensitic transformation or in the subsequent cycle (Fig. 10(d)). Massive transformations have been reported to occur during E-PBF, resulting in structures similar to that observed here, generally starting at a β GB [45].

4.2.3. Random (colony) evolution

It is clear in the case of the colony structure in the random scan strategy, that the microstructure transforms almost completely back to β. The colony structure is only observed when β transforms to α at a relatively slow cooling rate. A martensitic or basketweave structure does not transform to colonies directly [100]. Generally, if a basketweave structure is annealed below the β transus for long times, the observed behavior is coarsening and spheroidization [101–103]. With this in mind the regions which resemble basketweave in Fig. 7 (g,h) can be interpreted as coarsened primary α while the colonies are secondary α that formed after the martensite transformed back to β. So, the transformation most likely occurred as shown in Fig. 10(e), with the acicular α' transforming mostly back to β, with some α laths remaining, and then the β transforming into α+β colonies growing in from the GBs and around the retained primary α.

4.3. Comparison to steels

The results presented here have many interesting parallels to the literature on 3D characterization in steels described in the introduction. 3D characterization provided much valuable information on the

formation of Widmanstätten ferrite, bainite, and pearlite colonies. The advancement of serial sectioning and reconstruction capabilities now allows similar investigations in $\alpha+\beta$ titanium allows which exhibit many similar microstructural features on a finer length scale. On top of allowing a more detailed understanding of the phase evolution of Ti-6Al-4V during E-PBF, this reveals some new information about phase transformations in titanium alloys in general. The debate surrounding instability vs sympathetic nucleation in the formation of Widmanstätten structures in titanium is very similar to that in steels [4], although an interesting contrast is that here we see little evidence in favor of sympathetic nucleation. We show evidence of branching growth in the formation of the basketweave microstructure, similar to the branching behaviors observed in other titanium microstructures [50,54,55]. This suggests that the formation of this structure may have been diffusional while the formation of monolithic laths in the acicular structure was likely martensitic. This provides an interesting parallel to 3D studies on bainite structures which helped to unravel when the transformation was diffusional vs displacive [24,28,29,104]. The formation of colony α is similar to the formation of pearlite colonies [35,36,39,41] in many ways and likely also undergoes branching via morphological instability.

Conclusions

We present a detailed 3D investigation of the morphology, and particularly the interconnectivity, of three different microstructures produced by three different scanning strategies in Ti-6Al-4V during E-PBF. This information, which is unavailable using 2D characterization alone has provided several new insights into branching behavior in Ti-6Al-4V and its microstructural evolution following the martensitic transformation during initial rapid cooling.

1 The linear scan strategy results in a basketweave microstructure with extensive 3D interconnectivity. This microstructure may have formed directly from coarsened decomposed α', with interconnectivity arising solely from hard impingement or it may have formed as secondary α after a transformation back to β, with interconnectivity arising partially from morphological instability as platelets of different variants interact. The evidence for and against each case is discussed.
2 The Dehoff scan strategy at the bottom of the build results in an acicular microstructure consisting of individual α laths as well as large, interconnected clusters of allotriomorphic α. The interconnected allotriomorphic α may originate from a partial transformation back to β followed by a diffusional transformation to α with sympathetic nucleation or from a massive transformation during the initial cooling.
3 The random scan strategy results in colony microstructure that forms after a transformation back to β and has branching as a result of morphological instability.

These results have many parallels to similar phase transformations and microstructures in other complex alloy systems, such as steels, and illustrate the ways that 3D characterization can provide unique insight into microstructural evolution.

Declaration of Competing Interest

The authors declare that they have no known competing financial interests or personal relationships that could have appeared to influence the work reported in this paper.

Acknowledgments

The authors acknowledge gracefully support from the Department of Industry, Innovation and Science under the auspices of the AUSMURI program. The authors acknowledge the facilities, as well as the scientific and technical support of the Microscopy Australia node at UNSW Sydney (Mark Wainwright centre). The authors would also like to thank Prof. Sudarsanam Suresh Babu and Sabina Kumar at The University of Tennessee, Knoxville for providing materials, Prof. Peter Collins and Matthew Kenney at Iowa State University, Andrew Polonsky at The University of California, Santa Barbara, and Dr. Charlie Kong at UNSW Sydney for fruitful discussions, and Mike Jackson from BlueQuartz Software for support with the DREAM.3D software package. S. Primig is supported by the Australian Research Council DECRA (DE180100440) and UNSW Scientia Fellowship schemes.

Supplementary materials

Supplementary material associated with this article can be found, in the online version, at doi:10.1016/j.mtla.2021.101201.

References

[1] S.N. Monteiro, S. Paciornik, From historical backgrounds to recent advances in 3D characterization of materials: an overview, JOM 69 (2017) 84–92, doi:10.1007/s11837-016-2203-8.
[2] M.V. Kral, G. Spanos, Three dimensional morphology of cementite precipitates, Scr. Mater. 36 (1997) 875–882, doi:10.1016/S1359-6462(96)00498-8.
[3] M.V. Kral, G. Spanos, Three-dimensional analysis of proeutectoid cementite precipitates, Acta Mater. 47 (1999) 711–724, doi:10.1016/S1359-6454(98)00321-8.
[4] H.I. Aaronson, G. Spanos, R.A. Masamura, R.G. Vardiman, D.W. Moon, E.S.K. Menon, M.G. Hall, Sympathetic nucleation: an overview, Mater. Sci. Eng. B. 32 (1995) 107–123, doi:10.1016/0921-5107(95)80022-0.
[5] R.D. Townsend, J.S. Kirkaldy, Widmanstatten Ferrite Formation in Fe-C Alloys, Trans. Am. Soc. Met. 61 (1968) 605–619.
[6] H.I. Aaronson, C. Wells, Sympathetic Nucleation of Ferrite, JOM 8 (1956) 1216–1223, doi:10.1007/bf03377853.
[7] E.S.K. Menon, H.I. Aaronson, Overview no. 57 Morphology, crystallography and kinetics of sympathetic nucleation, Acta Metall. 35 (1987) 549–563, doi:10.1016/0001-6160(87)90179-9.
[8] K.C. Russell, D.M. Barnett, C.J. Altstetter, H.I. Aaronson, J.K. Lee, Strain energy interactions, the To concept and sympathetic nucleation, Scr. Metall. 11 (1977) 485–490, doi:10.1016/0036-9748(77)90162-4.
[9] W.W. Mullins, R.F. Sekerka, Stability of a planar interface during solidification of a dilute binary alloy, J. Appl. Phys. 35 (1964) 444–451, doi:10.1063/1.1713333.
[10] W.W. Mullins, R.F. Sekerka, Morphological Stability of a Particle Growing by Diffusion or Heat Flow, J. Appl. Phys. 34 (1963) 323–329, doi:10.1063/1.1702607.
[11] P.G. Shewmon, Interface Stability in Solid-Solid Transformations, Trans. Metall. Soc. AIME. 233 (1965) 736–748.
[12] G. Spanos, M.G. Hall, The formation mechanism(s), morphology, and crystallography of ferrite sideplates, Metall. Mater. Trans. A Phys. Metall. Mater. Sci. 27 (1996) 1519–1534, doi:10.1007/BF02649812.
[13] D. Phelan, R. Dippenaar, Widmanstätten ferrite plate formation in low-carbon steels, Metall. Mater. Trans. A Phys. Metall. Mater. Sci. 35 A (2004) 3701–3706, doi:10.1007/s11661-004-0276-4.
[14] D. Phelan, N. Stanford, R. Dippenaar, In situ observations of Widmanstätten ferrite formation in a low-carbon steel, Mater. Sci. Eng. A. 407 (2005) 127–134, doi:10.1016/j.msea.2005.07.015.
[15] K. Ameyama, G.C. Weatherly, K.T. Aust, A study of grain boundary nucleated widmanstätten precipitates in a two-phase stainless steel, Acta Metall. Mater. 40 (1992) 1835–1846, doi:10.1016/0956-7151(92)90170-J.
[16] J. Yin, M. Hillert, A. Borgenstam, Morphology of Proeutectoid Ferrite, Metall. Mater. Trans. A Phys. Metall. Mater. Sci. 48 (2017) 1425–1443, doi:10.1007/s11661-016-3903-y.
[17] M.A. MANGAN, P.D. LAUREN, G.J. SHIFLET, Three-dimensional reconstruction of Widmanstätten plates in Fe–12.3Mn–0.8C, J. Microsc. 188 (1997) 36–41, doi:10.1046/j.1365-2818.1997.2380799.x.
[18] M.V. Kral, G. Spanos, Three-dimensional analysis and classification of grain-boundary-nucleated proeutectoid ferrite precipitates, Metall. Mater. Trans. A Phys. Metall. Mater. Sci. 36 (2005) 1199–1207, doi:10.1007/s11661-005-0212-2.
[19] G. Spanos, A.W. Wilson, M.V. Kral, New insights into the widmanstätten proeutectoid ferrite transformation: integration of crystallographic and three-dimensional morphological observations, Metall. Mater. Trans. A Phys. Metall. Mater. Sci. 36 (2005) 1209–1218, doi:10.1007/s11661-005-0213-1.
[20] X.L. Wan, L. Cheng, K.M. Wu, Three-dimensional morphology and growth behavior of ferrite allotriomorphs formed at grain boundary edges, J. Iron Steel Res. Int. 17 (2010) 49–53, doi:10.1016/S1006-706X(10)60169-0.
[21] E. Eichen, H.I. Aaronson, G.M. Pound, R. Trivedi, Thermionic emission microscope study of the formation of ferrite sideplates, Acta Metall. 12 (1964) 1298–1301, doi:10.1016/0001-6160(64)90116-6.
[22] C.A. Dube, H.I. Aaronson, R.F. Mehl, La formation de la ferrite proeutectoïde dans les aciers au carbone, Rev. Métall. 55 (1958) 201–210, doi:10.1051/metal/195855030201.
[23] P. Dasgupta, The Nature of Ferrite in Iron-Nickel Meteorites, The Pennsylvania State University, 2011.
[24] L.C.D. Fielding, The Bainite controversy, Mater. Sci. Technol. 29 (2013) 383–399, doi:10.1179/1743284712Y.0000000157.

[25] J.W. Christian, Lattice correspondence, atomic site correspondence and shape change in “diffusional-displacive” phase transformations, Prog. Mater. Sci. 42 (1997) 101–108, doi:10.1016/s0079-6425(97)00009-1.

[26] W. Gong, Y. Tomota, Y. Adachi, A.M. Paradowska, J.F. Kelleher, S.Y. Zhang, Effects of ausforming temperature on bainite transformation, microstructure and variant selection in nanobainite steel, Acta Mater. 61 (2013) 4142–4154, doi:10.1016/j.actamat.2013.03.041.

[27] E. Keehan, L. Karlsson, H.K.D.H. Bhadeshia, M. Thuvander, Three-dimensional analysis of coalesced bainite using focused ion beam tomography, Mater. Charact. 59 (2008) 877–882, doi:10.1016/j.matchar.2007.07.011.

[28] J.S. Kang, J.B. Seol, C.G. Park, Three-dimensional characterization of bainitic microstructures in low-carbon high-strength low-alloy steel studied by electron backscatter diffraction, Mater. Charact. 79 (2013) 110–121, doi:10.1016/j.matchar.2013.02.009.

[29] S. Motomura, T. Hara, T. Omori, R. Kainuma, M. Nishida, Morphological and chemical analysis of bainite in Cu–17Al–11Mn (at.%) alloys by using orthogonal FIB-SEM and double-EDS STEM, Microscopy 65 (2016) 243–252, doi:10.1093/jmicro/dfw003.

[30] K.M. Wu, Y. Inagawa, M. Enomoto, Three-dimensional morphology of ferrite formed in association with inclusions in low-carbon steel, Mater. Charact. 52 (2004) 121–127, doi:10.1016/j.matchar.2004.04.004.

[31] S. Wu, C. Zhang, L. Zhu, Q. Zhang, X. Ma, In-depth analysis of intragranular acicular ferrite three-dimensional morphology, Scr. Mater. 185 (2020) 61–65, doi:10.1016/j.scriptamat.2020.03.007.

[32] R.A. Ricks, P.R. Howell, G. Barritte, The Nature of Acicular Ferrite in Steels, J. Mater. Sci. 17 (1982) 732–740.

[33] M. Díaz-Fuentes, I. Gutiérrez, Analysis of different acicular ferrite microstructures generated in a medium-carbon molybdenum steel, Mater. Sci. Eng. A. 363 (2003) 316–324, doi:10.1016/S0921-5093(03)00665-8.

[34] Z.G. Yang, J.B. Yang, H.S. Fang, B.Z. Bai, Theoretical study on sympathetic nucleation vs ledgewise growth of bainitic ferrite in steel, in: Mater. Sci. Forum, Trans Tech Publications Ltd, 2003: pp. 1261–1266. https://doi.org/10.4028/www.scientific.net/msf.426-432.1261.

[35] M. Hillert, The formation of pearlite, in: V.F. Zackay, H.I. Aaronson (Eds.), Decompos. Austenite by Diffus. Process., Interscience, New York, 1961, pp. 197–247.

[36] S.A. Hackney, G.J. Shiflet, Pearlite growth mechanism, Acta Metall. 35 (1987) 1019–1028, doi:10.1016/0001-6160(87)90049-6.

[37] S.A. Hackney, Morphological instabilities and branching processes at the initiation of the eutectoid transformation, Scr. Metall. Mater. 25 (1991) 1453–1458, doi:10.1016/0956-716X(91)90432-Z.

[38] D.L. Lee, C.G. Park, Sequential branching by ledge migration for the sidewise growth of pearlite, Scr. Metall. Mater. 32 (1995) 907–912, doi:10.1016/0956-716X(95)93223-Q.

[39] M.X. Zhang, P.M. Kelly, The morphology and formation mechanism of pearlite in steels, Mater. Charact. 60 (2009) 545–554, doi:10.1016/j.matchar.2009.01.001.

[40] I.K. Razumov, Stabilization of growth of a pearlite colony because of interaction between carbon and lattice dilatations, Phys. Solid State. 59 (2017) 1906–1912, doi:10.1134/S1063783417100304.

[41] M. De Graef, M.V. Kral, M. Hillert, A modern 3-D view of an “old” pearlite colony, JOM 58 (2006) 25–28, doi:10.1007/BF02748491.

[42] E.W. Collings, The Physical Metallury of Titanium Alloys, American Society for Metals, 1984.

[43] S. Nag, A. Devaraj, R. Srinivasan, R.E.A. Williams, N. Gupta, G.B. Viswanathan, J.S. Tiley, S. Banerjee, S.G. Srinivasan, H.L. Fraser, R. Banerjee, Novel mixed-mode phase transition involving a composition-dependent displacive component, Phys. Rev. Lett. 106 (2011) 245701, doi:10.1103/PhysRevLett.106.245701.

[44] T. Ahmed, H.J. Rack, Phase transformations during cooling in $\alpha + \beta$ titanium alloys, Mater. Sci. Eng. A. 243 (1998) 206–211, doi:10.1016/s0921-5093(97)00802-2.

[45] S.L. Lu, M. Qian, H.P. Tang, M. Yan, J. Wang, D.H. StJohn, Massive transformation in Ti-6Al-4V additively manufactured by selective electron beam melting, Acta Mater. 104 (2016) 303–311, doi:10.1016/j.actamat.2015.11.011.

[46] T. Zhang, D. Wang, Y. Wang, Novel transformation pathway and heterogeneous precipitate microstructure in Ti-alloys, Acta Mater. 196 (2020) 409–417, doi:10.1016/j.actamat.2020.06.048.

[47] A. Boyne, D. Wang, R.P. Shi, Y. Zheng, A. Behera, S. Nag, J.S. Tiley, H.L. Fraser, R. Banerjee, Y. Wang, Pseudospinodal mechanism for fine α/β microstructures in β-Ti alloys, Acta Mater. 64 (2014) 188–197, doi:10.1016/j.actamat.2013.10.026.

[48] L. Huang, Z. Sun, J. Cao, Z. Yin, The precipitation mechanism of secondary α-phase and formation of a bimodal microstructure in Ti6242S alloy cooled from the $\alpha + \beta$ phase field, J. Alloys Compd. 855 (2021) 157428, doi:10.1016/j.jallcom.2020.157428.

[49] Z. Sun, S. Guo, H. Yang, Nucleation and growth mechanism of α-lamellae of Ti alloy TA15 cooling from an $\alpha + \beta$ phase field, Acta Mater. 61 (2013) 2057–2064, doi:10.1016/j.actamat.2012.12.025.

[50] J. Sun, M. Qi, J. Zhang, X. Li, H. Wang, Y. Ma, D. Xu, J. Lei, R. Yang, Formation mechanism of α lamellae during $\beta \rightarrow \alpha$ transformation in polycrystalline dual-phase Ti alloys, J. Mater. Sci. Technol. 71 (2021) 98–108, doi:10.1016/j.jmst.2020.02.093.

[51] Z. Zhao, J. Chen, X. Lu, H. Tan, X. Lin, W. Huang, Formation mechanism of the α variant and its influence on the tensile properties of laser solid formed Ti-6Al-4V titanium alloy, Mater. Sci. Eng. A. 691 (2017) 16–24, doi:10.1016/j.msea.2017.03.035.

[52] B. Appolaire, L. Héricher, E. Aeby-Gautier, Modelling of phase transformation kinetics in Ti alloys - Isothermal treatments, Acta Mater. 53 (2005) 3001–3011, doi:10.1016/j.actamat.2005.03.014.

[53] M. Meng, X.G. Fan, H. Yang, L.G. Guo, M. Zhan, P.F. Gao, Precipitation of secondary alpha in competition with epitaxial growth of primary alpha in two-phase titanium alloys, J. Alloys Compd. 714 (2017) 294–302, doi:10.1016/j.jallcom.2017.04.209.

[54] H. Sharma, S.M.C. van Bohemen, R.H. Petrov, J. Sietsma, Three-dimensional analysis of microstructures in titanium, Acta Mater. 58 (2010) 2399–2407, doi:10.1016/j.actamat.2009.12.026.

[55] D. Choudhuri, R. Shi, A. Kashiwar, S. Dasari, R. Banerjee, D. Banerjee, α phase growth and branching in titanium alloys, PREPRINT. (2020). http://dx.doi.org/10.2139/ssrn.3681161.

[56] R. DeMott, P. Collins, C. Kong, X. Liao, S. Ringer, S. Primig, 3D electron backscatter diffraction study of α lath morphology in additively manufactured Ti-6Al-4V, Ultramicroscopy 218 (2020) 113073, doi:10.1016/j.ultramic.2020.113073.

[57] R. Williams, D. Bhattacharyya, G.B. Viswanathan, R. Banerjee, H.L. Fraser, Application of FIB-tomography to the study of microstructures in titanium alloys, in: Microscopy Microanalysis, Cambridge University Press, 2004, pp. 1178–1179, doi:10.1017/S1431927604884186.

[58] R.E.A. Williams, M. Uchic, D. Dimiduk, H.L. Fraser, Three dimensional reconstruction of alpha laths in α/β titanium alloys by serial sectioning with a FEI NOVA 600, in: Microscopy Microanalysis, Cambridge University Press, 2006, pp. 1234–1235, doi:10.1017/S1431927606066256.

[59] R.E.A. Williams, D. Huber, J. Sosa, H.L. Fraser, 15 years of characterizing titanium alloys’ microstructure by DBFIB, in: Microscopy Microanalysis, Cambridge University Press, 2014, pp. 322–323, doi:10.1017/S143192761400333X.

[60] T. Searles, J. Tiley, A. Tanner, R. Williams, B. Rollins, E. Lee, S. Kar, R. Banerjee, H.L. Fraser, Rapid characterization of titanium microstructural features for specific modelling of mechanical properties, Meas. Sci. Technol. 16 (2005) 60–69, doi:10.1088/0957-0233/16/1/009.

[61] S. Hémery, A. Naït-Ali, M. Guéguen, J. Wendorf, A.T. Polonsky, M.P. Echlin, J.C. Stinville, T.M. Pollock, P. Villechaise, A 3D analysis of the onset of slip activity in relation to the degree of micro-texture in Ti-6Al-4V, Acta Mater. (2019), doi:10.1016/j.actamat.2019.09.028.

[62] A. Kashiwar, 3D Microstructural Characterization in Some Alloys Using Serial Sectioning Techniques, IISc Bangalore, 2014 http://materials.iisc.ernet.in/~dbanerjee/assets/thesis_ankush.pdf (accessed May 2, 2019).

[63] J.S. Tiley, A.R. Shiveley, A.L. Pilchak, P.A. Shade, M.A. Groeber, 3D reconstruction of prior β grains in friction stir-processed Ti-6Al-4V, J. Microsc. 255 (2014) 71–77, doi:10.1111/jmi.12137.

[64] J. Ma, J. Tian, M. Yan, Z. Chen, J. Shen, J. Wu, Defect analysis and 2D/3D-EBSD investigation of an electron beam melted Ti-6Al-4V alloy, Mater. Charact. 166 (2020) 110440, doi:10.1016/j.matchar.2020.110440.

[65] D. He, S. Zaefferer, J. Zhu, Z. Lai, Three-dimensional morphological and crystallographic investigation of lamellar alpha and retained beta in a near alpha titanium alloy by combination of focused ion beam and electron backscattering diffraction, Steel Res. Int. (2012), doi:10.1002/srin.201200013.

[66] D.A. Hull, D. McCammond, D.W. Hoeppner, W.G. Hellier, Titanium prior-beta grain volume distribution by quantitative serial sectioning techniques, Mater. Charact. 26 (1991) 63–71, doi:10.1016/1044-5803(91)90067-E.

[67] N. Vanderesse, E. Maire, M. Darrieulat, F. Montheillet, M. Moreaud, D. Jeulin, Three-dimensional microtomographic study of Widmanstätten microstructures in an alpha/beta titanium alloy, Scr. Mater. 58 (2008) 512–515, doi:10.1016/j.scriptamat.2007.11.005.

[68] E. Wielewski, D.B. Menasche, P.G. Callahan, R.M. Suter, Three-dimensional colony characterization and prior-β grain reconstruction of a lamellar Ti-6Al-4V specimen using near-field high-energy X-ray diffraction microscopy, J. Appl. Crystallogr. 48 (2015) 1165–1171, doi:10.1107/S1600576715011139.

[69] Z. Jiao, J. Fu, Z. Li, X. Cheng, H. Tang, H. Wang, The spatial distribution of α phase in laser melting deposition additive manufactured Ti-10V-2Fe-3Al alloy, Mater. Des. 154 (2018) 108–116, doi:10.1016/j.matdes.2018.05.032.

[70] T.L. Burnett, R. Kelley, B. Winiarski, L. Contreras, M. Daly, A. Gholinia, M.G. Burke, P.J. Withers, Large volume serial section tomography by Xe Plasma FIB dual beam microscopy, Ultramicroscopy (2016), doi:10.1016/j.ultramic.2015.11.001.

[71] S.S. Al-Bermani, M.L. Blackmore, W. Zhang, I. Todd, The origin of microstructural diversity, texture, and mechanical properties in electron beam melted Ti-6Al-4V, Metall. Mater. Trans. A. 41 (2010) 3422–3434, doi:10.1007/s11661-010-0397-x.

[72] X. Tan, Y. Kok, Y.J. Tan, M. Descoins, D. Mangelinck, S.B. Tor, K.F. Leong, C.K. Chua, Graded microstructure and mechanical properties of additive manufactured Ti–6Al–4V via electron beam melting, Acta Mater. 97 (2015) 1–16, doi:10.1016/J.ACTAMAT.2015.06.036.

[73] X. Tan, Y. Kok, W.Q. Toh, Y.J. Tan, M. Descoins, D. Mangelinck, S.B. Tor, K.F. Leong, C.K. Chua, Revealing martensitic transformation and α/β interface evolution in electron beam melting three-dimensional-printed Ti-6Al-4V, Sci. Rep. 6 (2016) 1–10, doi:10.1038/srep26039.

[74] P.L. Stephenson, N. Haghdadi, R. DeMott, X.Z. Liao, S.P. Ringer, S. Primig, Effect of scanning strategy on variant selection in additively manufactured Ti-6Al-4V, Addit. Manuf. 36 (2020) 101581, doi:10.1016/j.addma.2020.101581.

[75] M.J. Quintana, M.J. Kenney, P. Agrawal, P.C. Collins, Texture analysis of additively manufactured Ti-6Al-4V deposited using different scanning strategies, Metall. Mater. Trans. A Phys. Metall. Mater. Sci. 51 (2020) 6574–6583, doi:10.1007/s11661-020-06040-4.

[76] M. Shao, S. Vijayan, P. Nandwana, J.R. Jinschek, The effect of beam scan strategies on microstructural variations in Ti-6Al-4V fabricated by electron beam powder bed fusion, Mater. Des. 196 (2020) 109165, doi:10.1016/j.matdes.2020.109165.

[77] N. Haghdadi, R. DeMott, P.L. Stephenson, X.Z. Liao, S.P. Ringer, S. Primig, Five-parameter characterization of intervariant boundaries in additively manufactured Ti-6Al-4V, Mater. Des. 196 (2020) 109177, doi:10.1016/j.matdes.2020.109177.

[78] R. DeMott, N. Haghdadi, X. Liao, et al., 3D characterization of microstructural evolution and variant selection in additively manufactured Ti-6Al-4V, J. Mater. Sci. 56 (2021) 14763–14782, doi:10.1007/s10853-021-06216-2.
[79] M.A. Groeber, M.A. Jackson, DREAM. 3D: a digital representation environment for the analysis of microstructure in 3D, Integr. Mater. Manuf. Innov. 3 (2014) 56–72, doi:10.1186/2193-9772-3-5.
[80] F. Bachmann, R. Hielscher, H. Schaeben, Texture analysis with MTEX- Free and open source software toolbox, in: Solid State Phenomenon, Trans Tech Publications Ltd, 2010, pp. 63–68, doi:10.4028/www.scientific.net/SSP.160.63.
[81] R. Subbarao, P. Meer, RANSAC Beyond, User independent robust regression, Proceeding of the IEEE Computer Society Conference on Computer Vision and Pattern Recognition, 2006, doi:10.1109/CVPRW.2006.43.
[82] P.H.S. Torr, A. Zisserman, Robust parameterization and computation of the trifocal tensor, Image Vis. Comput. 15 (1997) 591–605, doi:10.1016/s0262-8856(97)00010-3.
[83] D. Qiu, P. Zhao, R. Shi, Y. Wang, W. Lu, Effect of autocatalysis on variant selection of α precipitates during phase transformation in Ti-6Al-4V alloy, Comput. Mater. Sci. 124 (2016) 282–289, doi:10.1016/j.commatsci.2016.07.032.
[84] M. Tomellini, Soft impingement in diffusion-controlled growth of binary alloys: moving boundary effect in one-dimensional system, J. Mater. Sci. 48 (2013) 5653–5663, doi:10.1007/s10853-013-7361-2.
[85] K.E. Rajab, R.D. Doherty, Kinetics of growth and coarsening of faceted hexagonal precipitates in an f.c.c. matrix-I. Experimental observations, Acta Metall. 37 (1989) 2709–2722, doi:10.1016/0001-6160(89)90305-2.
[86] R.D. Doherty, K.E. Rajab, Kinetics of growth and coarsening of faceted hexagonal precipitates in an f.c.c. matrix-II, Analysis, Acta Metall. 37 (1989) 2723–2731, doi:10.1016/0001-6160(89)90306-4.
[87] A.K. Ackerman, A.J. Knowles, H.M. Gardner, A.A.N. Németh, I. Bantounas, A. Radecka, M.P. Moody, P.A.J. Bagot, R.C. Reed, D. Rugg, D. Dye, The kinetics of primary alpha plate growth in titanium alloys, Metall. Mater. Trans. A Phys. Metall. Mater. Sci. 51 (2020) 131–141, doi:10.1007/s11661-019-05472-x.
[88] X. Liu, H. Li, M. Zhan, Formation mechanism of lamellar alpha in titanium through accurate simulation, J. Alloys Compd. 811 (2019) 152085, doi:10.1016/j.jallcom.2019.152085.
[89] S.L. Semiatin, T.M. Lehner, J.D. Miller, R.D. Doherty, D.U. Furrer, Alpha/beta heat treatment of a titanium alloy with a nonuniform microstructure, Metall. Mater. Trans. A Phys. Metall. Mater. Sci. (2007) 910–921, doi:10.1007/s11661-007-9088-7.
[90] R.H. Buzolin, D. Weiß, A. Krumphals, M. Lasnik, M.C. Poletti, Modelling the competitive growth of primary, allotriomorphic, and secondary alpha in Ti-6Al-4V, Metall. Mater. Trans. A Phys. Metall. Mater. Sci. 51 (2020) 3967–3980, doi:10.1007/s11661-020-05810-4.
[91] M. Meng, H. Yang, X.G. Fan, S.L. Yan, A.M. Zhao, S. Zhu, On the modeling of diffusion-controlled growth of primary alpha in heat treatment of two-phase Ti-alloys, J. Alloys Compd. 691 (2017) 67–80, doi:10.1016/j.jallcom.2016.08.218.
[92] S.C. Wang, M. Aindow, M.J. Starink, Effect of self-accommodation on α/α boundary populations in pure titanium, Acta Mater. 51 (2003) 2485–2503, doi:10.1016/S1359-6454(03)00035-1.
[93] I. Katzarov, S. Malinov, W. Sha, Finite element modeling of the morphology of β to α phase transformation in Ti-6Al-4V alloy, Metall. Mater. Trans. A Phys. Metall. Mater. Sci. 33 (2002) 1027–1040, doi:10.1007/s11661-002-0204-4.
[94] S. Malinov, Z. Guo, W. Sha, A. Wilson, Differential scanning calorimetry study and computer modeling of $\beta \Rightarrow \alpha$ phase transformation in a Ti-6Al-4V alloy, Metall. Mater. Trans. A Phys. Metall. Mater. Sci. 32 (2001) 879–887, doi:10.1007/s11661-001-0345-x.
[95] S. Malinov, P. Markovsky, W. Sha, Z. Guo, Resistivity study and computer modelling of the isothermal transformation kinetics of Ti-6Al-4V and Ti-6Al-2Sn-4Zr-2Mo-0.08Si alloys, J. Alloys Compd. 314 (2001) 181–192, doi:10.1016/S0925-8388(00)01227-5.
[96] D. Qiu, R. Shi, P. Zhao, D. Zhang, W. Lu, Y. Wang, Effect of low-angle grain boundaries on morphology and variant selection of grain boundary allotriomorphs and Widmanstätten side-plates, Acta Mater. 112 (2016) 347–360, doi:10.1016/j.actamat.2016.04.033.
[97] S.S. Babu, S.M. Kelly, E.D. Specht, T.A. Palmer, J.W. Elmer, Measurement of phase transformation kinetics during repeated thermal cycling of TI-6AL-4V using time resolved x-ray diffraction, in: J.M. Howe, D.E. Laughlin, J.K. Lee, U. Dahmen, W.A. Soffa (Eds.), Solid-Solid Phase Transformations in Inorganic Materials 2005 Vol. 2, 2005: pp. 503–508.
[98] S.M. Kelly, S.L. Kampe, Microstructural evolution in laser-deposited multilayer Ti-6Al-4V builds: part 1. Microstructural characterization, Metall. Mater. Trans. A Phys. Metall. Mater. Sci. 35 A (2004) 1861–1867, doi:10.1007/s11661-004-0094-8.
[99] S.M. Kelly, S.L. Kampe, Microstructural evolution in laser-deposited multilayer Ti-6Al-4V builds: part II. Thermal Modeling, Metall. Mater. Trans. A Phys. Metall. Mater. Sci. 35 A (2004) 1869–1879. https://doi.org/10.1007/s11661-004-0095-7.
[100] S. Zhang, Y. Gao, G. Wang, Y. Liu, R. Yang, Growth+behavior+of+α+phase+in+Ti-5.6Al-4.8Sn-2.0Zr-1.0Mo-0.35Si-0.7Nd+titanium+alloy.pdf, J. Mater. Sci. Technol 22 (2006) 459–464.
[101] C.L. Li, J.K. Hong, P.L. Narayana, S.W. Choi, S.W. Lee, C.H. Park, J.T. Yeom, Q. Mei, Realizing superior ductility of selective laser melted Ti-6Al-4V through a multi-step heat treatment, Mater. Sci. Eng. A. 799 (2021) 140367, doi:10.1016/j.msea.2020.140367.
[102] S. Balachandran, A. Kashiwar, A. Choudhury, D. Banerjee, R. Shi, Y. Wang, On variant distribution and coarsening behavior of the α phase in a metastable β titanium alloy, Acta Mater. 106 (2016) 374–387, doi:10.1016/J.ACTAMAT.2016.01.023.
[103] P. Barriobero-Vila, K. Artzt, A. Stark, N. Schell, M. Siggel, J. Gussone, J. Kleinert, W. Kitsche, G. Requena, J. Haubrich, Mapping the geometry of Ti-6Al-4V: from martensite decomposition to localized spheroidization during selective laser melting, Scr. Mater. 182 (2020) 48–52, doi:10.1016/j.scriptamat.2020.02.043.
[104] H.I. Aaronson, M.G. Hall, A history of the controversy over the roles of shear and diffusion in plate formation above Md and a comparison of the atomic mechanisms of these processes, Metall. Mater. Trans. A. 25 (1994) 1797–1819, doi:10.1007/BF02649030.